

# Single-Stage Three-Phase AC–AC Matrix Converter for Inductive Power Transfer Systems

Masood Moghaddami, *Student Member, IEEE*, Arash Anzalchi, *Student Member, IEEE*, and Arif I. Sarwat, *Member, IEEE*

**Abstract**—A direct three-phase ac–ac matrix converter for inductive power transfer (IPT) systems with soft-switching operation is introduced. The proposed topology is expected to have a high reliability and extended lifetime due to the soft-switching operation and elimination of short-life electrolytic capacitors. The soft-switching operation will also reduce switching stress, switching loss, and electromagnetic interference of the converter. A variable-frequency control strategy based on the energy-injection and free-oscillation technique is used to regulate the resonant current, the resonant voltage, and the output power. With the use of reverse-blocking switches, the proposed converter can be built with a reduced number of switches (only seven), which will consequently increase the reliability and efficiency and reduce the cost of the converter. The converter operates in eight modes, which are described in detail. With the use of the proposed converter as the primary converter, simulation analysis and experimental implementations on a case study IPT system show that the current regulation control method can fully regulate the output current and output power around user-defined reference values, thus making it suitable for dynamic IPT applications, where the system has inherent variations.

**Index Terms**—AC–AC converter, inductive power transfer (IPT), matrix converter, soft switching.

## I. INTRODUCTION

INDUCTIVE power transfer (IPT) systems are emerging technology for transferring electric power to a variety of applications without any physical contacts. This technology transfers power from one system to another across a large air gap and through a loosely coupled inductive link. It also offers high efficiency typically between 85% and 90% and robustness. Furthermore, it offers high reliability, even when used in hazardous environments, as it is not affected by dust or chemicals, and eliminates sparking and the risk of electrical shock [1], [2]. Therefore, it is a safe, vigorous, and clean way of transferring power and has rapidly increased interest in commercial and industrial applications. The IPT technology has been successfully employed in many applications, including systems for material handling [3], [4], biomedical implants, and transportation systems [5], [6]. Specifically, this innovative technology can be

Manuscript received November 30, 2015; revised March 9, 2016; accepted April 6, 2016. Date of publication May 5, 2016; date of current version September 9, 2016. This work was supported by the National Science Foundation under Grant CRISP-1541108.

The authors are with the Department of Electrical and Computer Engineering, Florida International University, Miami, FL 33174 USA (e-mail: mmogh003@fiu.edu; aanza005@fiu.edu; asarwat@fiu.edu).

Color versions of one or more of the figures in this paper are available online at <http://ieeexplore.ieee.org>.

Digital Object Identifier 10.1109/TIE.2016.2563408

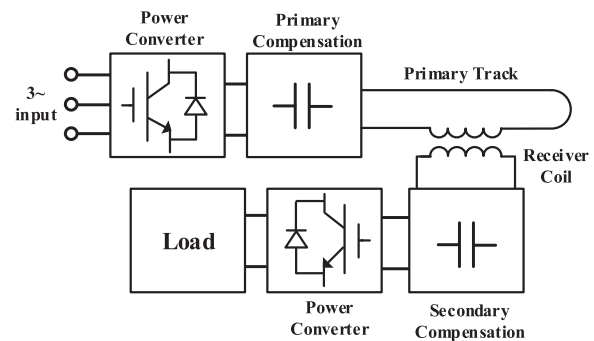


Fig. 1. Typical loosely coupled IPT system.

used for static and dynamic wireless power transfer for electric vehicles (EVs) [1], [7].

A typical configuration of an IPT system is shown in Fig. 1. In a loosely coupled IPT system, the inductive link requires a strong magnetic field to be created to deliver high-power levels at large air gaps due to weak coupling of the coils. To achieve this, this technology requires the use of power converters to achieve that can generate large currents at high frequencies, often in the kilohertz range (10–58 kHz). In order to generate a high-frequency current on the primary side, specific power converters are employed in IPT systems. Power converters play a key role in the performance of IPT systems. Recent developments in IPT systems have heightened the need for high-power, reliable, and efficient converters. Normally, these converters take 50/60 Hz current from mains and convert to high-frequency using an ac–dc–ac two-stage power conversion. The power source of an IPT system is usually the electric utility (single-phase or three-phase) supplying power at 50/60 Hz.

Voltage-source inverters based on pulse width modulation with a front-end rectifier have become the preferred choice for most practical applications [8]. This is mainly due to their simple topology and low cost. On the other hand, this two-stage topology has low-frequency harmonics on the dc link and the ac input line, which requires the use of very bulky short-life electrolytic capacitors for the dc link and a large low-pass filter at the output [8]. Several topologies have been proposed to solve the problems of the traditional ac–dc–ac power converters [9]–[11]. Matrix converters are the main alternatives for two-stage converters that can convert energy directly from an ac source to a load with different frequency and amplitude without any energy storage elements [12]. These converters have the advantages of the simple and compact topology, bidirectional power flow capability, high-quality input-current waveforms, and adjustable

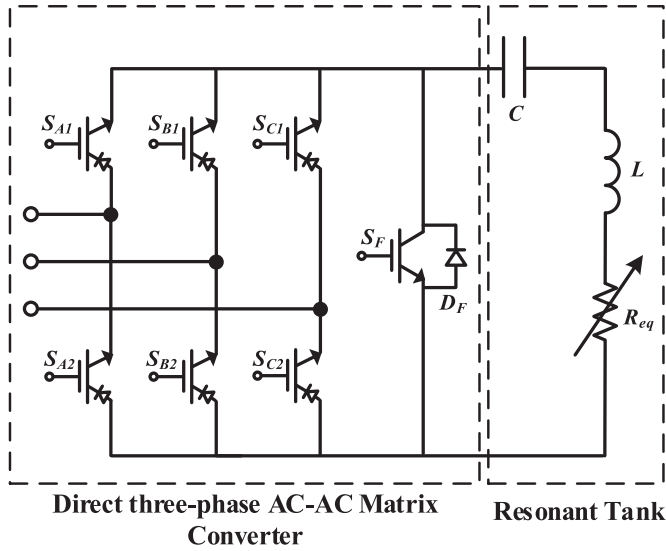


Fig. 2. Proposed three-phase ac-ac matrix converter.

input power factor independent of the load [8], [12]–[15]. Particularly, different converter topologies have been proposed for IPT applications [16]–[24]. A simple, compact, and highly efficient single-phase matrix converter for IPT applications is presented in [16]. The energy-injection and free-oscillation control strategy is applied to the topology. However, this matrix converter suffers from current sags around input ac voltage zero crossings.

In this paper, a new three-phase ac-ac matrix converter for IPT systems is proposed. The proposed matrix topology can be built using seven switches, in which six are reverse-blocking switches and one is a regular switch. A variable-frequency control strategy based on the proposed converter is used, which is based on the energy-injection and free-oscillation technique. The key benefits of the proposed converter are soft-switching operation, high efficiency, reduced number of switches, and low electromagnetic interference.

## II. PROPOSED THREE-PHASE AC-AC CONVERTER

The proposed direct three-phase ac-ac converter is shown in Fig. 2. In this figure,  $C$  represents the primary compensation capacitor,  $L$  is the primary self-inductance, and  $R_{eq}$  is the reflected resistance of the load at the secondary to the primary circuit. The proposed converter consists of six reverse-blocking switches and one regular switch (insulated-gate bipolar transistor (IGBT) or MOSFET) which is in parallel with the resonant tank. A reverse-blocking switch can be built using a series combination of an IGBT or a MOSFET with a diode. However, individual switches with reverse-blocking capability are now available in the market and have the advantage of total lower forward voltage. Thereby, enabling the converter to operate with higher efficiency.

In [16], a control strategy for a single-phase ac-ac converter based on energy-injection and free oscillation of the resonant circuit is presented. This control method is further developed in this study and is applied for three different control modes,

TABLE I  
SWITCHING STATES IN DIFFERENT MODES OF OPERATION IN CURRENT REGULATION CONTROL MODE

Mode	Resonant Current	Input Voltages	Conducting Switches
1	$i_p < 0,  i_p  < i_{ref}$	$V_b < V_c < V_a$	$S_{A1}, S_{B2}$
2	$i_p < 0,  i_p  < i_{ref}$	$V_c < V_b < V_a$	$S_{A1}, S_{C2}$
3	$i_p < 0,  i_p  < i_{ref}$	$V_a < V_c < V_b$	$S_{B1}, S_{A2}$
4	$i_p < 0,  i_p  < i_{ref}$	$V_c < V_a < V_b$	$S_{B1}, S_{C2}$
5	$i_p < 0,  i_p  < i_{ref}$	$V_b < V_a < V_c$	$S_{C1}, S_{B2}$
6	$i_p < 0,  i_p  < i_{ref}$	$V_a < V_b < V_c$	$S_{C1}, S_{A2}$
7	$i_p < 0,  i_p  > i_{ref}$	–	$D_F$
8	$i_p > 0$	–	$S_F$

TABLE II  
SWITCHING STATES IN DIFFERENT MODES OF OPERATION IN VOLTAGE REGULATION CONTROL MODE

Mode	Resonant Voltage & Current	Input Voltages	Conducting Switches
1	$v_p < 0,  v_p  < v_{ref}$	$V_b < V_c < V_a$	$S_{A1}, S_{B2}$
2	$v_p < 0,  v_p  < v_{ref}$	$V_c < V_b < V_a$	$S_{A1}, S_{C2}$
3	$v_p < 0,  v_p  < v_{ref}$	$V_a < V_c < V_b$	$S_{B1}, S_{A2}$
4	$v_p < 0,  v_p  < v_{ref}$	$V_c < V_a < V_b$	$S_{B1}, S_{C2}$
5	$v_p < 0,  v_p  < v_{ref}$	$V_b < V_a < V_c$	$S_{C1}, S_{B2}$
6	$v_p < 0,  v_p  < v_{ref}$	$V_a < V_b < V_c$	$S_{C1}, S_{A2}$
7	$v_p < 0,  v_p  > v_{ref}$	–	$D_F$
8	$i_p > 0$	–	$S_F$

which are resonant current regulation control, power regulation control, and resonant voltage regulation control. The control modes are all based on zero-current switching (ZCS) operation. Since the proposed converter is based on the resonant current zero-crossing points, the operating frequency of the converter is equal to the resonant current frequency (natural damped frequency, which is described in Section III). Therefore, the operating frequency of the converter is determined by the circuit parameters. In a dynamic IPT system, the primary and secondary self-inductances are fixed by the track/coil parameters, such as size and number of turns in the coil. In practice, although the primary's position relative to secondary affects the mutual inductance, it has a very small effect on self-inductances; due to the inherently large air gaps required in EV dynamic charging systems, such variations are minimized. Therefore, self-inductances of the primary ( $L$  in Fig. 2) and secondary are constant. This ensures the performance of the converter in dynamic IPT systems.

The operation of the converter for each control mode can be described in eight operation modes, which are presented in Tables I–III. The operation modes 1–6 are energy-injection modes in which energy is injected to the  $LC$  tank, and the operation modes 7 and 8 are free-oscillation modes in which the  $LC$  tank continues its resonant oscillation. The transition of different modes of operation occurs at current zero-crossing points. Each mode starts at a resonant current zero crossing and continues for a half-cycle until the next resonant current zero crossing. This operation mode transition is determined based on the state of the circuit, as well as the user-defined reference

**TABLE III**  
SWITCHING STATES IN DIFFERENT MODES OF OPERATION IN POWER REGULATION CONTROL MODE

Mode	Output Power & Resonant Current	Input Voltages	Conducting Switches
1	$P_{out} < P_{ref}, i_p < 0$	$V_b < V_c < V_a$	$S_{A1}, S_{B2}$
2	$P_{out} < P_{ref}, i_p < 0$	$V_c < V_b < V_a$	$S_{A1}, S_{C2}$
3	$P_{out} < P_{ref}, i_p < 0$	$V_a < V_c < V_b$	$S_{B1}, S_{A2}$
4	$P_{out} < P_{ref}, i_p < 0$	$V_c < V_a < V_b$	$S_{B1}, S_{C2}$
5	$P_{out} < P_{ref}, i_p < 0$	$V_b < V_a < V_c$	$S_{C1}, S_{B2}$
6	$P_{out} < P_{ref}, i_p < 0$	$V_a < V_b < V_c$	$S_{C1}, S_{A2}$
7	$P_{out} > P_{ref}, i_p < 0$	–	$D_F$
8	$i_p > 0$	–	$S_F$

values for the resonant current, the resonant voltage, and the output power.

### A. Current Regulation Control Mode

The resonant current regulation plays a key role in the power transfer performance of an IPT system. Since the resonant current amplitude is proportional to the amount of injected energy to the  $LC$  tank, the resonant current regulation control can be achieved by continuously changing the operation mode of the converter from energy-injection modes (increasing the resonant current) to free-oscillation modes (decreasing the resonant current), and vice versa. Using this strategy, the resonant current can be regulated around a user-defined reference current. This is carried out by comparing the peak output resonant current  $i_p$  to the reference current ( $i_{ref}$ ) at each current zero-crossing point. The  $i_p$  is measured in each half-cycle of the resonant current. If  $i_p$  is negative and its absolute value is less than  $i_{ref}$  ( $i_p < 0$  and  $|i_p| < i_{ref}$ ), an energy injection to the  $LC$  tank is required for the next half-cycle to increase the resonant current. According to Table I, the converter should enter one of the energy-injection modes 1–6, depending on the three-phase input voltages. Moreover, if  $i_p$  is positive or its absolute value is more than  $i_{ref}$  ( $i_p > 0$  or  $|i_p| > i_{ref}$ ), the converter should enter one of the free-oscillation modes 7 and 8. A conceptual plot of three-phase input voltages, resonant current, and corresponding switching signals of the converter in different modes of operations is presented in Fig. 3. Also, Fig. 4 demonstrates the resonant current path in the proposed converter in eight modes of operation.

In each energy-injection mode, the  $LC$  tank terminals are switched between the most positive and the most negative input lines. According to Table I, the switching is performed using six reverse-blocking switches,  $S_{A1}, S_{A2}, S_{B1}, S_{B2}, S_{C1}$ , and  $S_{C2}$ , which are used to switch the three-phase input lines to the output during modes 1–6, based on the measured input voltages. It should be noted that the energy injection always occurs in positive half-cycles of the resonant current. In free-oscillation modes, the negative half-cycles of the resonant current are conducted through the parallel switch  $S_F$  (mode 8) and the positive half-cycles of the resonant current are conducted through the intrinsic body diode  $D_F$  (mode 7). It should be noted that negative half-cycles are always free-oscillation modes; therefore,  $S_F$  is switched at the rate of the resonance frequency. Since the

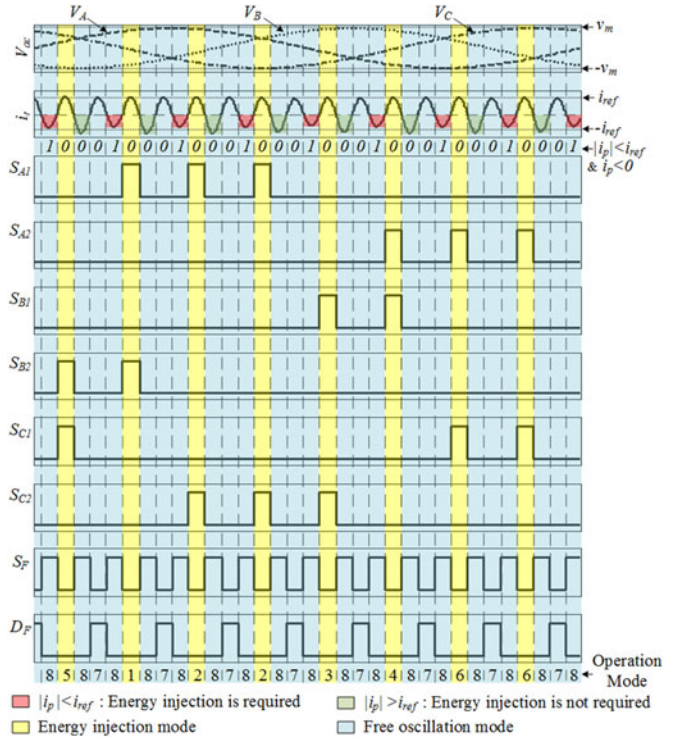


**Fig. 3.** Conceptual plot of three-phase input voltages, resonant current, and corresponding switching signals of the converter in different modes of operations.

resonant current becomes negative after any mode from 1 to 7, mode 8 always occurs after any other mode of operation.

### B. Voltage Regulation Control Mode

The voltage limit in the  $LC$  tank and particularly in the compensation capacitor is of great importance. This voltage limit is mostly limited to the insulation level of the primary coils/tracks and voltage rating of the compensation capacitor. The voltage regulation control can be achieved using an approach similar to the current regulation control mode. In Section III, it is shown that the peak resonant voltage occurs in each resonant current zero crossing. Therefore, the resonant voltage can be measured in each current zero crossing and peak voltage detection is not required.

In voltage regulation control mode, if the peak resonant voltage is negative and its absolute value is lower than the reference voltage ( $v_p < 0$  and  $|v_p| < v_{ref}$ ), then according to Table III, the circuit will enter one of the energy-injection modes 1–6, depending on the three-phase input voltages. Therefore, energy will be injected to the  $LC$  tank for a half-cycle to increase the resonant voltage, and the  $LC$  tank terminals are switched between the most positive and the most negative input lines. The switching is performed using six switches,  $S_{A1}, S_{A2}, S_{B1}, S_{B2}, S_{C1}$ , and  $S_{C2}$ , which are used to switch the three-phase input lines to the output during modes 1–6, according to Table II and based on the measured input voltages. Mode 7 occurs when the peak voltage is negative and its absolute value is higher than the reference voltage ( $v_p < 0$  and  $|v_p| > v_{ref}$ ), and therefore,

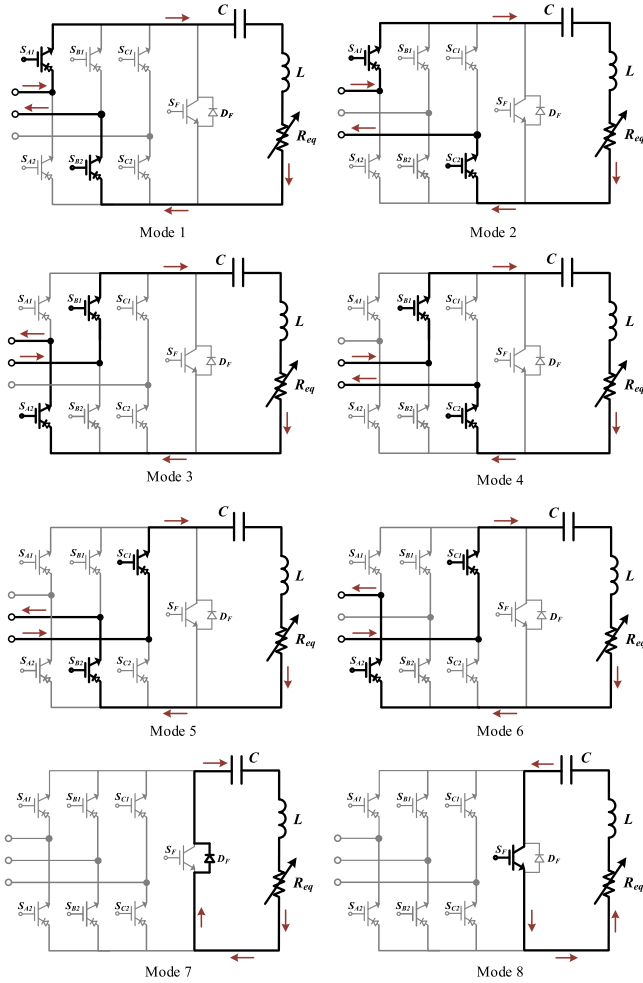


Fig. 4. Current path in the proposed converter in eight modes of operation.

energy injection to  $LC$  tank should be avoided for a half-cycle to decrease the resonant voltage. In this mode, the  $LC$  tank enters a free-oscillation state and the resonant current is positive, which is conducted through the intrinsic body diode ( $D_F$ ) of the parallel switch ( $S_F$ ) as shown in Fig. 4 for mode 7. In mode 8, the resonant current is negative and the switch  $S_F$  is ON. Since the resonant current becomes negative after any mode between 1 and 7, mode 8 always occurs after any other mode of operation.

### C. Power Regulation Control Mode

In dynamic IPT systems due to inherent variations in the load, power transfer control is important. The power input regulation control can be achieved using an approach similar to the current regulation control method. The peak current ( $i_p$ ) and the input voltage ( $V_{in}$ ) are measured. Considering the fact that all negative half-cycles are free-oscillation modes, and in free-oscillation modes, the input voltage is zero ( $V_{in} = 0$ ), the average output power ( $P_{in}$ ) for a full-cycle ( $T$ ) can be calculated as follows:

$$P_{out} = \int_T i_p V_{in} = \frac{1}{\pi} i_p V_{in}. \quad (1)$$

In this control mode, in each current zero crossing,  $P_{out}$  is compared to a reference power ( $P_{ref}$ ), and if the average output power ( $P_{out}$ ) in one half-cycle is lower than the reference power ( $P_{ref}$ ), the circuit will enter one of the energy-injection modes 1–6, depending on the three-phase input voltages based on Table III. Therefore, energy will be injected to the  $LC$  tank in the next half-cycle to increase the resonant current, and the  $LC$  tank terminals are switched between the most positive and the most negative input lines. According to Table III, the switching is performed using six switches,  $S_{A1}$ ,  $S_{A2}$ ,  $S_{B1}$ ,  $S_{B2}$ ,  $S_{C1}$ , and  $S_{C2}$ , which are used to switch the three-phase input lines to the output during modes 1–6, based on the measured input voltages. Mode 7 occurs when the average output power ( $P_{out}$ ) is higher than the reference power ( $P_{ref}$ ); therefore, energy injection to  $LC$  tank should be avoided for a half-cycle to decrease the resonant current. In this mode, the  $LC$  tank enters a free-oscillation state and the resonant current is positive, which is conducted through the intrinsic body diode ( $D_F$ ) of the parallel switch ( $S_F$ ), as shown in Fig. 4 for mode 7. In mode 8, the resonant current is negative and the switch  $S_F$  is ON. Since the resonant current becomes negative after any mode between 1 and 7, mode 8 always occurs after any other mode of operation.

### III. THEORETICAL ANALYSIS

The differential equation of an  $LC$  tank with primary self-inductance of  $L$  and compensation capacitor  $C$  with an equivalent resistance of  $R_{eq}$  can be expressed as

$$L \frac{di}{dt} + R_{eq} i + \frac{1}{C} \int_0^t i dt + v_c(0) = V_t \quad (2)$$

where  $i$  is the resonant current,  $v_c$  is the voltage of the compensation capacitor, and  $V_t$  is the input voltage. Equation (2) can be rewritten as the following second-order differential equation:

$$\frac{d^2 i}{dt^2} + \frac{R_{eq}}{L} \frac{di}{dt} + \frac{1}{LC} i = 0 \quad (3)$$

where the initial conditions of the circuit are

$$i(0) = 0 \quad (4)$$

$$L \frac{di}{dt}(0) = V_t - v_c(0).$$

The solution of (3) based on initial conditions in (4) is derived as

$$i = K e^{-t/\tau} \sin(\omega t) \quad (5)$$

where the natural damped frequency  $\omega = \sqrt{\omega_0^2 - \alpha^2}$ , resonant frequency  $\omega_0 = 1/\sqrt{LC}$ , damping coefficient  $\alpha = R_{eq}/2L$ , damping time constant  $\tau = 2L/R$ , and the coefficient  $K$  is expressed as

$$K = \frac{V_t - v_c(0)}{\omega L}. \quad (6)$$

Equation (5) shows that the peak current decreases exponentially with a time constant of  $\tau$  and (6) shows that the value of  $K$  changes in each half-cycle depending on the input voltage and initial voltage of the compensation capacitor. It should be noted that in the free-oscillation modes, the input voltage is

zero ( $V_i = 0$ ). Also the compensation capacitor voltage can be expressed as

$$v_c(t) = v_c(0) + \frac{K\tau}{C(1 + \tau^2 \omega^2)} \left( \tau\omega - e^{-t/\tau} [\sin(\omega t) + \tau\omega \cos(\omega t)] \right). \quad (7)$$

The resonant current and voltage equations (5) and (7) can be used for finding the peak values of current and voltage in each half-cycle. In order to find the peak value of the resonant current  $i_n$ , which occurs at the time  $t_n$  corresponding to the  $n$ th current peak, the following equation can be solved to find the extremum points of the resonant current:

$$\frac{di}{dt} = K e^{-t/\tau} \left[ \omega \cos(\omega t) - \frac{1}{\tau} \sin(\omega t) \right] = 0. \quad (8)$$

By simplifying (8), the following equations are derived:

$$\tan(\omega t_n) = \tau\omega \quad (9)$$

$$t_n = \frac{\text{atan}(\tau\omega) + n\pi}{\omega}. \quad (10)$$

Therefore, the  $n$ th peak value of the resonant current can be calculated using (5) and (10) as the following equation:

$$i_n = K e^{-\frac{\text{atan}(\tau\omega) + n\pi}{\tau\omega}} (-1)^n \frac{\tau\omega}{\sqrt{1 + (\tau\omega)^2}}. \quad (11)$$

Similarly, the peak values of the resonant voltage can be found using (7) as follows:

$$\frac{dv_c}{dt} = -\frac{K\tau e^{-t/\tau}}{C(1 + \tau^2 \omega^2)} \left( [\omega \cos(\omega t) - \tau\omega^2 \sin(\omega t)] - \frac{1}{\tau} [\sin(\omega t) + \tau\omega \cos(\omega t)] \right) = 0. \quad (12)$$

Equation (12) can be simplified as following set of equations:

$$\frac{dv_c}{dt} = \frac{K}{C} e^{-t/\tau} \sin(\omega t) = 0 \quad (13)$$

$$\sin(\omega t_n) = 0 \quad (14)$$

$$t_n = \frac{n\pi}{\omega}. \quad (15)$$

Based on (5), (13), (14), and (15), it can be seen that in each resonant current zero crossing, resonant voltage is exactly in its peak. Since control modes, which are presented in Section II, are all based on resonance current zero-crossing points, the voltage regulation control mode can be established on peak values of resonant voltage in each current zero crossing.

Using (5), the resonant current in a time period composed of both energy-injection and free-oscillation modes can be expressed as follows:

$$i(t) = \begin{cases} K_i e^{-t/\tau} \sin(\omega t), & 0 < t < \frac{\pi}{\omega} \\ K_f e^{-t/\tau} \sin(\omega t), & \frac{\pi}{\omega} < t < \frac{2m\pi}{\omega} \end{cases} \quad (16)$$

where  $m$  denotes the number of cycles, which is composed of one energy-injection half-cycle and  $2m - 1$  free-oscillation half-cycles, and  $K_i$  and  $K_f$  are coefficients of (5) in the first

energy-injection and free-oscillation half-cycles, respectively, and can be calculated using (6) and (7) as follows:

$$K_i = \frac{1}{\omega L} [V_i - v_c(0)] \quad (17)$$

$$K_f = \frac{1}{\omega L} \left[ v_c \left( \frac{\pi}{\omega} \right) \right] = \frac{1}{\omega L} \left[ v_c(0) + \frac{K_i \tau^2 \omega}{C(1 + \tau^2 \omega^2)} \left( 1 + e^{-\pi/\tau\omega} \right) \right]. \quad (18)$$

By assuming  $i_{\text{ref}}$  as the reference current, using (11) and (12), the number of cycles that the next energy injection should occur ( $m$ ) can be calculated as follows:

$$m = \frac{1}{\pi} \left[ \tau\omega \ln \left( \frac{K_f \tau\omega}{i_{\text{ref}} \sqrt{1 + (\tau\omega)^2}} \right) + \arctan(\tau\omega) \right]. \quad (19)$$

Equation (19) predicts the number of cycles that the  $LC$  tank will continue its free-oscillation mode, after an energy-injection mode, as a function of initial condition ( $K_f$ ), circuit parameters ( $\tau\omega$ ), and the reference current  $i_{\text{ref}}$ . A duty cycle can be defined as the ratio of the number of energy-injection modes to the number of free-oscillation modes in the time interval between two successive energy-injection modes and can be written as follows:

$$D_i = \frac{1}{m + 1} = \frac{f_{\text{inj}}}{f_r} \quad (20)$$

where  $f_{\text{inj}}$  is the switching frequency of the energy-injection modes and  $f_r$  is the resonance frequency of the  $LC$  tank. The duty cycle  $D_i$  is a measure that represents the energy demand for the  $LC$  tank. For example, in Fig. 3, this measure is  $D_i = 0.5$ , which shows that only half of the cycles energy needs to be injected to the  $LC$  tank.

### A. Converter Loss Analysis

The power loss of the proposed converter can be calculated by evaluating the conduction and switching losses of the power switches in different modes of operation. The loss of each power switch is composed of switching and conduction losses and can be written as follows:

$$P_{Sx} = P_{S\text{con}} + P_{S\text{sw}} = [V_F I_{\text{avg}} + R_F I_{\text{rms}}^2] T_{\text{con}} f_{\text{sw}} + \left[ (E_{\text{on}} + E_{\text{off}}) + \frac{1}{2} C_{\text{oss}} V_{\text{in}}^2 \right] f_{\text{sw}} \quad (21)$$

where  $P_{S\text{cond}}$  and  $P_{S\text{sw}}$  are the conduction and switching losses of the switch  $S_x$ , respectively,  $V_F$  is the forward voltage of the power switch (in power MOSFETs,  $V_F = 0$ ),  $R_F$  is the equivalent resistance of the switch during on state,  $I_{\text{avg}}$  and  $I_{\text{rms}}$  are the mean and RMS values of the conducted current, respectively,  $T_{\text{con}}$  is the conduction time of the switch,  $f_{\text{sw}}$  is the switching frequency,  $E_{\text{on}}$  and  $E_{\text{off}}$  are volt-ampere crossover energy losses during the switch turn-on and turn-off transitions, respectively,  $C_{\text{oss}}$  is the output capacitance of the switch, and  $V_{\text{in}}$  is the input voltage. Since in the converter benefits from ZCS switching are always performed, the switching losses from

TABLE IV

TYPICAL VALUES FOR PARAMETERS USED FOR THEORETICAL CONVERTER LOSS CALCULATION

Parameter	Description	Typical Value
$V_F$	Switch forward voltage	1.5 V
$R_F$	Equivalent on-state resistance	0.08 $\Omega$
$C_{oss}$	Output capacitance	250 pF
$E_{on} + E_{off}$	Switching volt-ampere crossover energy losses	2 mJ
$V_{FD}$	Diode forward voltage	1.8 V
$E_{rr}$	Reverse recovery energy loss	200 $\mu$ J

volt-ampere crossover are minimized and, thus, are relatively low. Therefore, the conduction losses dominate, followed by the losses due to  $C_{oss}$  (output losses). The losses associated with any diode in the converter are composed of conduction and reverse recovery losses and can be calculated as follows:

$$P_{D_x} = P_{D_{cond}} + P_{D_{rr}} = V_{FD} I_{avg} T_{con} f_{sw} + E_{rr} f_{sw} \quad (22)$$

where  $P_{D_{cond}}$  and  $P_{D_{rr}}$  are the conduction and reverse recovery losses of the diode  $D_x$ , respectively,  $V_{FD}$  is the forward voltage of the diode, and  $E_{rr}$  is the reverse recovery energy of the diode. The losses of the converter can be calculated by calculation of the losses associated with energy-injection and free-oscillation modes separately, considering the fact that the switching frequency of all the switches is  $f_{inj} = D_i f_r$ , except  $S_F$  which its switching frequency is  $f_r$ . In each energy-injection mode (modes 1–6), two reverse-blocking switches are involved; therefore, the losses associated with energy-injection modes ( $P_{inj}$ ) can be described as follows:

$$P_{inj} = 2D_i(P_{S_x} + P_{D_x}). \quad (23)$$

It should be noted that if the switches  $S_{A1}$ ,  $S_{A2}$ ,  $S_{B1}$ ,  $S_{B2}$ ,  $S_{C1}$ , and  $S_{C2}$  are switches with built-in reverse-blocking capability,  $P_{D_x}$  loss is eliminated in (23), and as a result, the efficiency of the converter will be increased. Since  $S_F$  and its body diode  $D_F$  are the only switches, involved in free-oscillation modes, the losses associated with free-oscillation modes ( $P_{osc}$ ) can be calculated as follows:

$$P_{osc} = P_{S_x} + D_i P_{D_x}. \quad (24)$$

Finally, the total dissipated power can be described as follows:

$$P_{loss} = P_{inj} + P_{osc}. \quad (25)$$

Typical values for high-power switches and diodes for 50-A output current are presented in Table IV. However, for different values of current, these typical values should be modified accordingly. Fig. 6 presents the efficiency of the converter versus resonant current and switching frequency, which is calculated based on Table IV and (21)–(25). This figure shows that the efficiency of the converter increases as the resonant current increases, and any change in the switching frequency does not affect the efficiency significantly in high resonant currents. Also, the maximum efficiency of the converter is 96.6%.

## IV. SIMULATION RESULTS

The proposed three-phase converter, which is presented in Fig. 2, is simulated using MATLAB/Simulink. The IPT model is shown in Fig. 5. This model is composed of a three-phase power supply with an output  $LC$  filter, the primary three-phase ac-ac converter, the primary and secondary magnetic structures with their corresponding compensation capacitors, and the secondary load, which is a battery charger of an EV. The controller of the primary converter and its components are also shown in Fig. 5. The measurements include the three-phase input voltage and the output resonant current of the  $LC$  tank. The controller is triggered in each resonant current zero crossing, and based on the voltage and current measurements, the switching state of the of the converter is determined. The switching signals of the converter do not change until the next current zero crossing.

The self-inductances of the primary and secondary are each 168  $\mu$ H, where each have a 1- $\mu$ F compensation capacitor, and thereby, the operating frequency of the converter, which is equal to the resonance frequency of the  $LC$  tank, would be 12.28 kHz. The line-to-line voltage of the three-phase supply is 208 V. The current regulation control mode is enabled with 282.8-A (200-Arms) reference current. The simulation results including the three-phase input voltages and their corresponding modes of operation, the output resonant current, and corresponding switching signals of  $S_{A1}$ ,  $S_{B1}$ ,  $S_{C2}$ ,  $S_F$  are shown in Fig. 7. Also, the frequency spectrum of the output resonant current is shown in Fig. 8. As can be seen in Figs. 7 and 8, the current is fully regulated around the reference current and its total harmonic distortion (THD) is 9.22%. The active and reactive power calculations show that the total output power is 18.4 kW, and the fundamental reactive power is zero ( $Q_1 = 0$ ), and therefore, the displacement power factor is unity (DPF = 1). However, due to higher order harmonics in the three-phase input voltages and currents, the true power factor is 0.76. Using the specifications given in Table IV for the switches of the converter, the efficiency of the converter is calculated based on (21)–(25) through the simulation, which is 96.2%.

## V. EXPERIMENTAL RESULTS

The experimental study is performed on a case study IPT system, which is shown in Fig. 9. This system is composed of two circular magnetic structures with 700-mm diameter and 200-mm air gap. The circular power pads are composed of coils, ferrite bars, and aluminum shields. The proposed three-phase matrix converter is used as the primary converter with a series-parallel topology, which is shown in Fig. 5 is implemented, where the self-inductance of each circular pad is 168  $\mu$ H, and 1- $\mu$ F compensation capacitors are used in both primary and secondary circuits. The line voltage of the three-phase power supply is 40 V. In this experimental study, series combination of a MOSFET (IRF3205) with a diode (DSEP 30-12A) is used to make the reverse the blocking switches. However, switches with built-in reverse-blocking capability are available in the market (e.g., IXRH-40N120). The switch  $S_F$  is also an IRF3205 MOSFET, and its body diode is used as the diode  $D_F$ . A STM32F4-

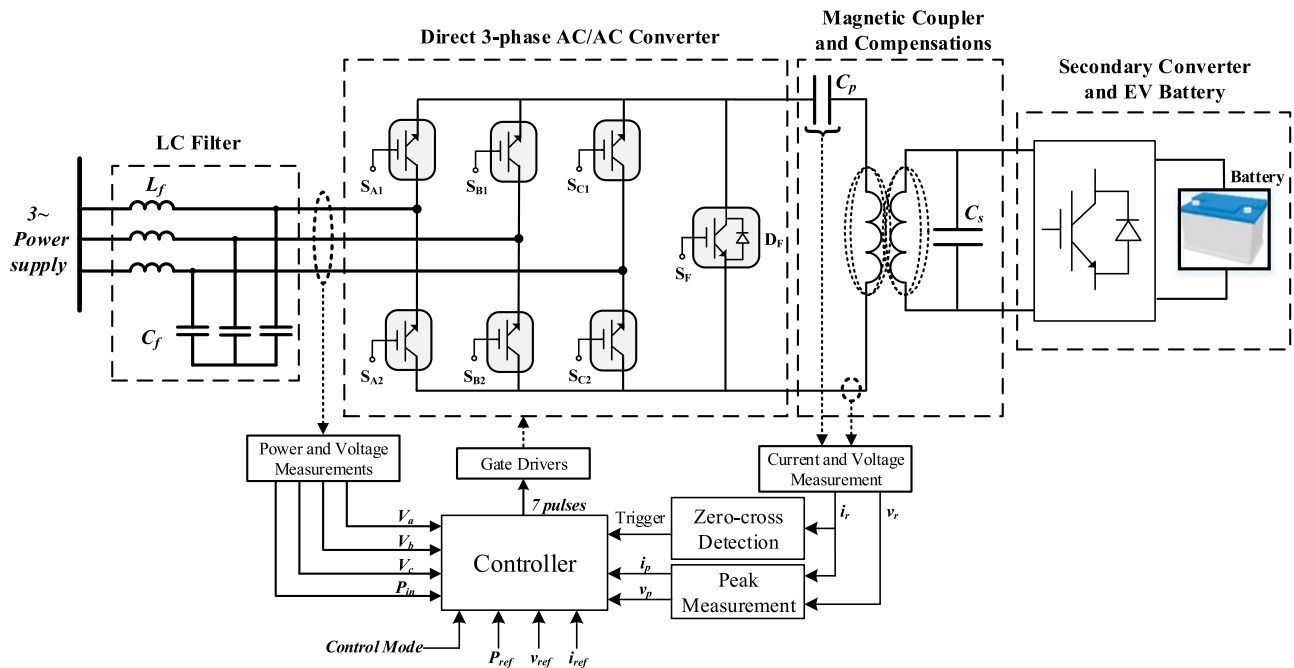


Fig. 5. IPT model and its components simulated in MATLAB/Simulink.

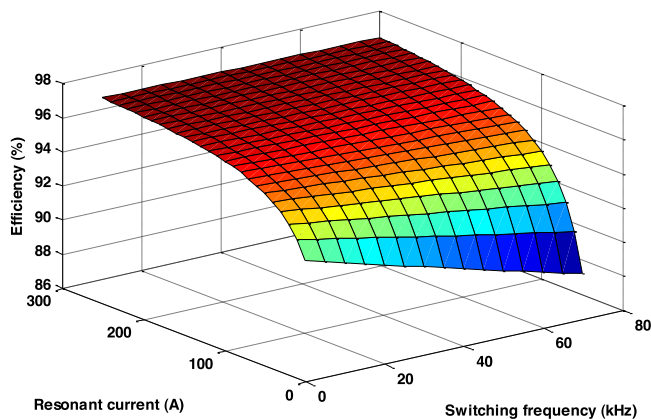


Fig. 6. Efficiency of the converter versus switching frequency ( $f_{sw}$ ) and resonant current ( $i_r$ ), calculated analytically.

discovery board with an ARM Cortex-M4 168-MHz DSP is used as the main controller. The resonant current regulation and output power regulation control strategies are studied on the case study IPT system, which are described below.

### A. Current Regulation Control

The resonant current regulation control with 14.1-A (10-Arms) reference current is used to regulate the resonance current. Fig. 10 shows the output resonant current and corresponding switching signals of  $S_{A1}$ ,  $S_{B1}$ , and  $S_F$  switches during the transition of the most positive phase in voltage from phase A to phase B. The operating frequency of the converter is 12.25 kHz, which has a small discrepancy compared to the theoretical resonance frequency (12.28 kHz). The waveforms of the input

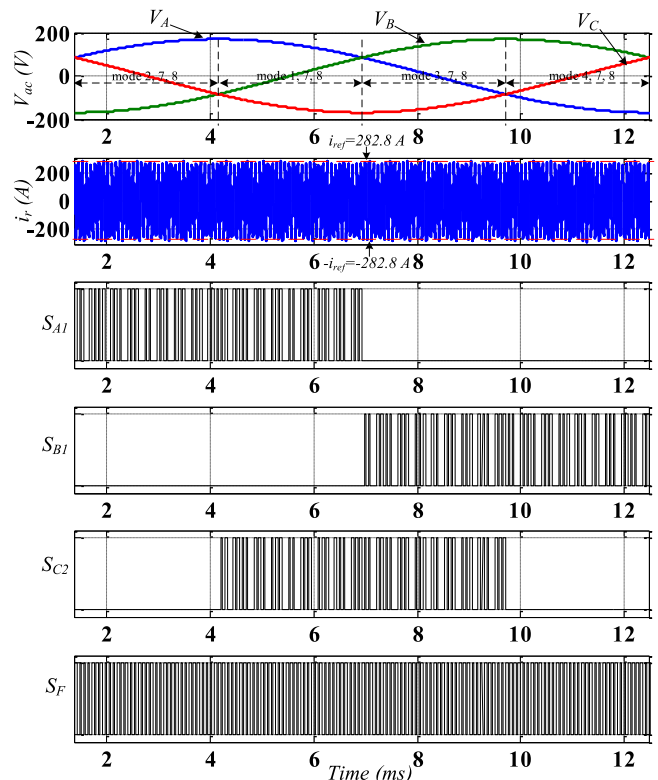


Fig. 7. Simulation results of the IPT system with  $i_{ref} = 282.8$  A.

voltage ( $V_a$ ), input current ( $i_a$ ), input power ( $P_{out}$ ) for phase A, and output resonant current are shown in Fig. 11. As can be seen, the resonant current is fully regulated around the reference current. However, the input voltage has high-frequency

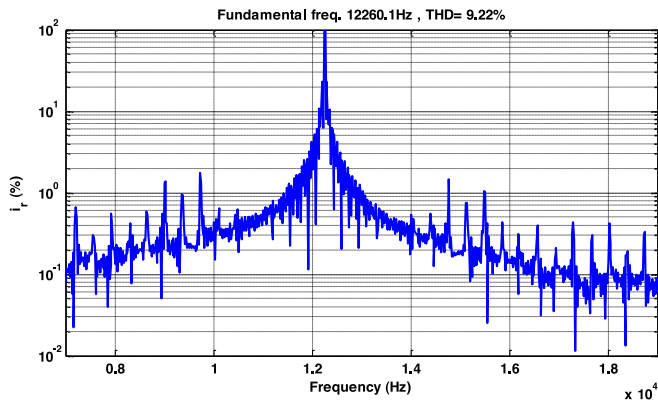


Fig. 8. Frequency spectrum of the resonant current shown in Fig. 6.

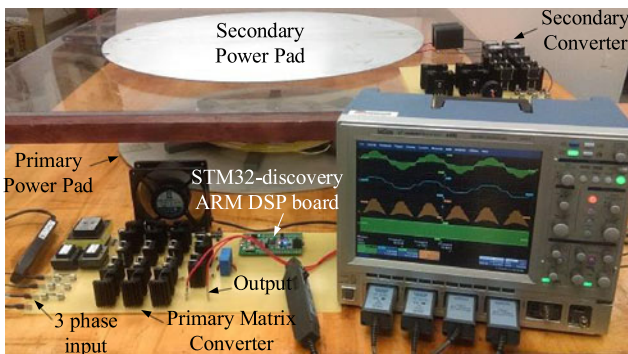


Fig. 9. Case study IPT system with circular power pads.

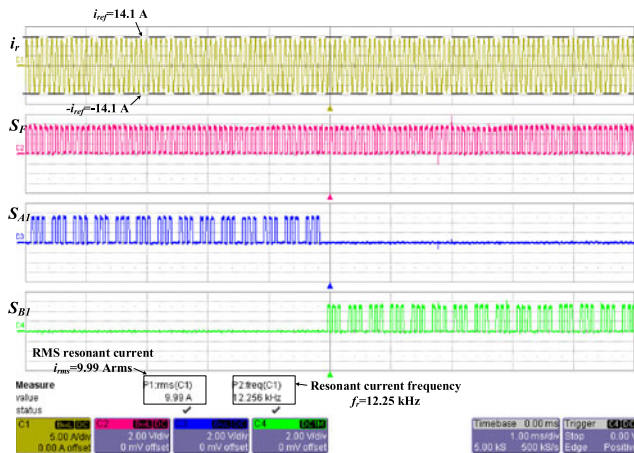


Fig. 10. Experimental results on the case study IPT system: Output resonant current and corresponding switching signals.

harmonics, which will reduce the true power factor of the converter; as a result, it also will reduce the power transfer efficiency of the converter. The frequency spectrum of the output resonant current is measured experimentally, which is shown in Fig. 12. Calculations show that the THD of the output resonant current is 14.3%. The total output power is 267 W (89 W from each phase). The input power factor measurements show that the true power factor is 0.67. However, the fundamental reactive power

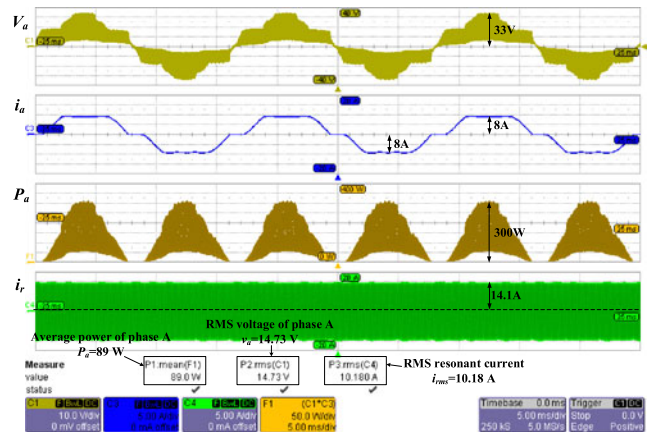


Fig. 11. Experimental results on the case study IPT system: input voltage ( $V_a$ ), input current ( $i_a$ ), and power ( $P_a$ ) for phase A, and output resonant current ( $i_r$ ).

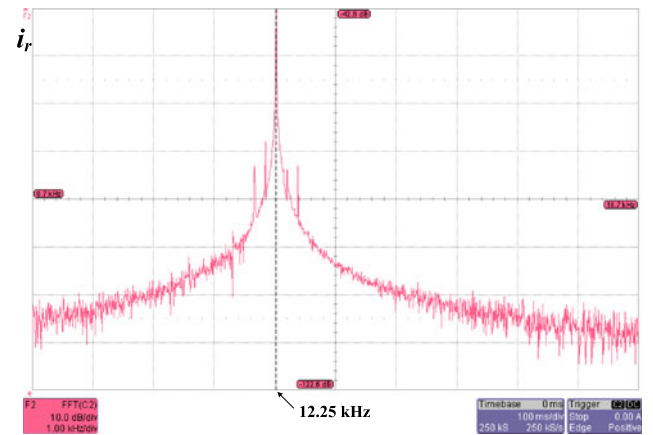


Fig. 12. Frequency spectrum of the resonant current shown in Fig. 9.

is zero, and therefore, the displacement power factor is unity. Also, the measured loss of the converter is 31.5 W, and consequently, the efficiency of the converter is 89.4% compared to 92.7% theoretical efficiency using (21)–(25).

## B. Power Regulation Control

The output power control mode with 130-W reference power is used to regulate the output power. The output power and the output resonant current are shown in Fig. 13. Similar to the current regulation control, the operating frequency of the converter is 12.25 kHz. While the average output power ( $P_{Out}$ ) is maintained at 136.4 W, the peak instantaneous output power is 510 W and the RMS resonant current is 7.81 A. The true power factor and displacement power factor are 0.59 and 1, respectively. Measurements show that the total converter loss is 25.1 W, and as a result, the efficiency of the converter is 84.46% compared to 87.9% theoretical efficiency using (21)–(25).

The main limiting factors in the proposed converter are the speed of the controller (DSP board) and the response delay time of the resonant current measurement. In IPT applications,

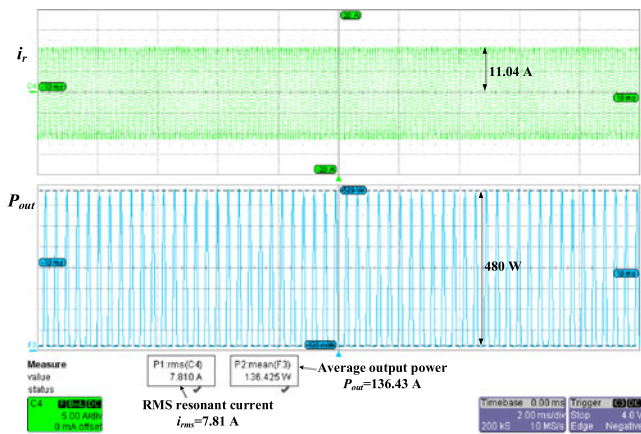


Fig. 13. Output power and the resonant current using the power regulation control with  $P_{ref} = 60$  W.

high-frequency operation of the converter (10–85 kHz) is essential to maximize the power transfer efficiency. On the other hand, in the proposed converter, the current and voltage measurements using analog-to-digital conversion (ADC), with high sampling rate are required. Also, the implemented control strategy on the DSP, which consist of floating-point operations and comparisons, etc., along with ADC conversions, will take tens of clock cycles of the DSP to execute. As a result, a DSP with a high clock speed is essential. The maximum frequency that can be practically achieved using the DSP board (STM32F4-discovery ARM Cortex-M4 168 MHz DSP) is about 40 kHz. However, the proposed controller of the converter has the potential to be implemented based on analog circuit, which can significantly enhance the controller speed and resolve the need for a DSP.

Also, a Hall-effect current transducer “LA 55-P” is used for the resonant current measurement, which has a response delay less than  $1 \mu\text{s}$ . Considering the fact that at least 20 samples in a full-cycle of the resonant current are required for a proper performance of the converter (without losing the zero-crossing points), the maximum frequency that practically can be achieved is about 50 kHz based on the response time delay of the current measurement.

## VI. CONCLUSION

This paper has introduced a novel three-phase single-stage ac–ac converter for IPT systems. The proposed converter has different control modes, which can be used to regulate the resonant current, resonant voltage, and output power around user-defined reference values. The energy-injection and free-oscillation control strategy provides a simple and effective method, which makes it suitable for the control of IPT systems. Key benefits of the proposed converter are the minimized number of switches, soft-switching operation, and elimination of short-life electrolytic capacitors. These features will lead to a high-efficiency converter with high reliability and extended lifetime. With the use of reverse-blocking switches, the converter can be built only with seven switches. The simulation results and

experimental studies show that the proposed converter can maintain the resonant current or the output power around the user-defined reference values. This feature makes this converter suitable for dynamic IPT systems, where the system has inherent variations. The experimental studies on a case study IPT system show that the converter can provide a resonant current with 14.3% THD. However, the efficiency of the converter is low in low power (88.2% at 267 W); theoretical efficiency calculations show that in higher powers, the converter can reach efficiency as high as 96.6%.

## REFERENCES

- [1] C.-S. Wang, O. H. Stielau, and G. A. Covic, “Design considerations for a contactless electric vehicle battery charger,” *IEEE Trans. Ind. Electron.*, vol. 52, no. 5, pp. 1308–1314, Oct. 2005.
- [2] S. Y. R. Hui and W. W. C. Ho, “A new generation of universal contactless battery charging platform for portable consumer electronic equipment,” *IEEE Trans. Power Electron.*, vol. 20, no. 3, pp. 620–627, May. 2005.
- [3] J. de Boeij, E. A. Lomonova, and A. J. A. Vandenput, “Optimization of contactless planar actuator with manipulator,” *IEEE Trans. Magn.*, vol. 44, no. 6, pp. 1118–1121, Jun. 2008.
- [4] P. Sergeant and A. V. D. Bossche, “Inductive coupler for contactless power transmission,” *IET Elect. Power Appl.*, vol. 2, no. 1, pp. 1–7, Jan. 2008.
- [5] G. Wang, W. Liu, M. Sivaprakasam, and G. A. Kendir, “Design and analysis of an adaptive transcutaneous power telemetry for biomedical implants,” *IEEE Trans. Circuits Syst. I, Reg. Papers*, vol. 52, no. 10, pp. 2109–2117, Oct. 2005.
- [6] P. Li and R. Bashirullah, “A wireless power interface for rechargeable battery operated medical implants,” *IEEE Trans. Circuits Syst. II, Exp. Briefs*, vol. 54, no. 10, pp. 912–916, Oct. 2007.
- [7] O. H. Stielau and G. A. Covic, “Design of loosely coupled inductive power transfer systems,” in *Proc. Int. Conf. Power Syst. Technol.*, 2000, vol. 1, pp. 85–90.
- [8] R. Lai *et al.*, “A systematic topology evaluation methodology for high-density three-phase PWM ac-ac converters,” *IEEE Trans. Power Electron.*, vol. 23, no. 6, pp. 2665–2680, Nov. 2008.
- [9] B.-G. Gu and K. Nam, “A dc-link capacitor minimization method through direct capacitor current control,” *IEEE Trans. Ind. Appl.*, vol. 42, no. 2, pp. 573–581, Mar./Apr. 2006.
- [10] L. Li and D. Tang, “Cascade three-level ac/ac direct converter,” *IEEE Trans. Ind. Electron.*, vol. 59, no. 1, pp. 27–34, Jan. 2012.
- [11] L. Malesani, L. Rossetto, P. Tenti, and P. Tomasin, “Ac/dc/ac PWM converter with reduced energy storage in the dc link,” *IEEE Trans. Ind. Appl.*, vol. 31, no. 2, pp. 287–292, Mar. 1995.
- [12] P. W. Wheeler, J. Rodriguez, J. C. Clare, L. Empringham, and A. Weinstein, “Matrix converters: a technology review,” *IEEE Trans. Ind. Electron.*, vol. 49, no. 2, pp. 276–288, Apr. 2002.
- [13] J. W. Kolar, T. Friedli, J. Rodriguez, and P. W. Wheeler, “Review of three-phase PWM ac-ac converter topologies,” *IEEE Trans. Ind. Electron.*, vol. 58, no. 11, pp. 4988–5006, Nov. 2011.
- [14] J. Rodriguez, M. Rivera, J. W. Kolar, and P. W. Wheeler, “A review of control and modulation methods for matrix converters,” *IEEE Trans. Ind. Electron.*, vol. 59, no. 1, pp. 58–70, Jan. 2012.
- [15] H. Keyhani and H. A. Toliyat, “A soft-switched three-phase ac-ac converter with a high-frequency ac link,” *IEEE Trans. Ind. Appl.*, vol. 50, no. 4, pp. 2637–2647, Jul./Aug. 2014.
- [16] H. L. Li, A. P. Hu, and G. A. Covic, “A direct ac-ac converter for inductive power-transfer systems,” *IEEE Trans. Power Electron.*, vol. 27, no. 2, pp. 661–668, Feb. 2012.
- [17] U. K. Madawala and D. J. Thrimawithana, “Current sourced bi-directional inductive power transfer system,” *IET Power Electron.*, vol. 4, no. 4, pp. 471–480, Apr. 2011.
- [18] C.-S. Wang, G. A. Covic, and O. H. Stielau, “Investigating an LCL load resonant inverter for inductive power transfer applications,” *IEEE Trans. Power Electron.*, vol. 19, no. 4, pp. 995–1002, Jul. 2004.
- [19] C. Y. Huang, J. T. Boys, and G. A. Covic, “LCL pickup circulating current controller for inductive power transfer systems,” *IEEE Trans. Power Electron.*, vol. 28, no. 4, pp. 2081–2093, Apr. 2013.
- [20] S. Aldhafer, P. C. K. Luk, A. Bati, and J. F. Whidborne, “Wireless power transfer using class e inverter with saturable dc-feed inductor,” *IEEE Trans. Ind. Appl.*, vol. 50, no. 4, pp. 2710–2718, Jul./Aug. 2014.

- [21] Z. Pantic, S. Bai, and S. M. Lukic, "ZCS LCC-compensated resonant inverter for inductive-power-transfer application," *IEEE Trans. Ind. Electron.*, vol. 58, no. 8, pp. 3500–3510, Aug. 2011.
- [22] J. I. Rodriguez and S. B. Leeb, "A multilevel inverter topology for inductively coupled power transfer," *IEEE Trans. Power Electron.*, vol. 21, no. 6, pp. 1607–1617, Nov. 2006.
- [23] N. A. Keeling, G. A. Covic, and J. T. Boys, "A unity-power-factor IPT pickup for high-power applications," *IEEE Trans. Ind. Electron.*, vol. 57, no. 2, pp. 744–751, Feb. 2010.
- [24] M. G. Egan, D. L. O'Sullivan, J. G. Hayes, M. J. Willers, and C. P. Henze, "Power-factor-corrected single-stage inductive charger for electric vehicle batteries," *IEEE Trans. Ind. Electron.*, vol. 54, no. 2, pp. 1217–1226, Apr. 2007.



**Masood Moghaddami** (S'15) received the B.S. degree from Amirkabir University of Technology, Tehran, Iran, in 2009, and the M.S. degree from Iran University of Science and Technology, Tehran, in 2012. He is currently working toward the Ph.D. degree in the Department of Electrical and Computer Engineering, Florida International University, Miami, FL, USA.

From 2011 to 2014, he worked in industry as an Engineer designing optimization of large power transformers. His research interests include finite-element analysis, power electronics, contactless power transfer, and renewable energy systems.



**Arash Anzalchi** (S'14) received the B.S. degree from K.N. Toosi University of Technology, Tehran, Iran, and the M.S. degree from the Science and Research Branch, Islamic Azad University, Tehran, in 2007 and 2011, respectively, both in electrical engineering. He is currently working toward the Ph.D. degree at Florida International University, Miami, FL, USA, as a Graduate Research Assistant.

He is also one of the researchers of the Energy Power Reliability and Analytic Center, which conducts high-end studies on the effect of high-penetration PV integration into the smart grid. His research interests include PV integration into the distribution grid, mitigation of power quality issues, and smart power electronic technologies for renewable energy sources.



**Arif I. Sarwat** (M'08) received the M.S. degree in electrical and computer engineering from the University of Florida, Gainesville, FL, USA, in 2005, and the Ph.D. degree in electrical engineering from the University of South Florida, Tampa, FL, USA, in 2010.

He worked in the industry (SIEMENS) for nine years, executing many critical projects. Currently, he is an Assistant Professor in the Department of Electrical and Computer Engineering, Florida International University (FIU), Miami, FL, USA, where he leads the Energy, Power and Sustainability (EPS) group. Before joining FIU, he was Assistant Professor of Electrical Engineering at the University at Buffalo, State University of New York (SUNY). His significant work in energy storage, microgrid, and DSM is demonstrated by Sustainable Electric Energy Delivery Systems in Florida. His research areas are smart grids, high-penetration renewable systems, power system reliability, large-scale distributed generation integration, large-scale data analysis, and vehicular technology.

Dr. Sarwat was the recipient of an NSF CAREER Award in 2015.